

# Uncertainty of temperature measurements by infrared thermography for metal cutting applications

B Lane<sup>1</sup>, E Whitenton<sup>1</sup>, V Madhavan<sup>1,2</sup> and A Donmez<sup>1</sup>

<sup>1</sup> National Institute of Standards and Technology, Gaithersburg, MD, USA

<sup>2</sup> Industrial and Manufacturing Engineering Department, Wichita State University, Wichita, KS, USA

E-mail: [brandon.lane@nist.gov](mailto:brandon.lane@nist.gov)

Received 29 May 2013, in final form 2 October 2013

Published 12 November 2013

Online at [stacks.iop.org/Met/50/637](http://stacks.iop.org/Met/50/637)

## Abstract

This paper presents a comprehensive analysis of the uncertainty in the measurement of the peak temperature on the side face of a cutting tool, during the metal cutting process, by infrared thermography. The analysis considers the use of a commercial off-the-shelf camera and optics, typical of what is used in metal cutting research. A physics-based temperature measurement equation is considered and an analytical method is used to propagate the uncertainties associated with measurement variables to determine the overall temperature measurement uncertainty. A Monte Carlo simulation is used to expand on the analytical method by incorporating additional sources of uncertainty such as a point spread function (PSF) of the optics, difference in emissivity of the chip and tool, and motion blur. Further discussion is provided regarding the effect of sub-scene averaging and magnification on the measured temperature values. It is shown that a typical maximum cutting tool temperature measurement results in an expanded uncertainty of  $U = 50.1\text{ }^{\circ}\text{C}$  ( $k = 2$ ). The most significant contributors to this uncertainty are found to be uncertainties in cutting tool emissivity and PSF of the imaging system.

(Some figures may appear in colour only in the online journal)

## 1. Introduction

Industry continually strives to optimize metal cutting processes so that parts may be made faster, better and at less cost. One of the important factors to consider when optimizing metal cutting processes is the maximum temperature of the cutting tool, which is widely regarded as a key variable affecting the wear of the cutting tool. Many researchers use infrared (IR) thermography to measure cutting tool temperatures. Although specially designed equipment exists for this purpose (e.g. NIST-developed dual-spectrum system [1, 2]), commercial off-the-shelf (COTS) thermal cameras are increasingly used due to their wider field of view and smaller size. This paper represents an effort to better understand uncertainties associated with using a COTS IR camera to measure tool temperatures during metal cutting. The COTS camera used in this investigation has a lens with 50 mm focal length and a 15 mm extension tube. The central quarter of the focal

plane array (FPA) produces an image 160 pixels wide and 128 pixels high, corresponding to a field of view 6 mm wide and 4.8 mm high. The frame rate is 800 frames per second and the integration time typically used is 25  $\mu\text{s}$ . The optical filter has a 3.9  $\mu\text{m}$  centre wavelength with 0.2  $\mu\text{m}$  bandpass.

Many research efforts using IR thermography to measure temperature in metal cutting are available in the literature [3–5]. While a few discuss the uncertainty associated with their respective measuring instruments and setups, many describe the measurement as being generally imprecise. However, the ability to obtain whole temperature fields at and near the cutting point without contact or interaction with the process makes IR thermography an alluring technique. In their review, Davies *et al* [4] discussed generally agreed principles regarding uncertainty in metal cutting thermography: (1) emissivity is typically the largest contributor to uncertainty, and (2) square of the error increases proportionally with detector wavelength, the square of temperature, and in inverse proportion to the

square of emissivity. Whittenton [1, 2] identified many of the uncertainty sources in metal cutting thermography during the development of the NIST high-speed dual-spectrum imaging system. Whittenton's work focused on uncertainty sources associated with the unique environmental effects such as radiation polarization, motion blur, point spread function (PSF), micro-blackbodies and cavities, oxidation and dynamic change to emissivity, size of source error and more. However, it did not give a systematic method for arriving at a combined uncertainty value for a particular temperature measurement scenario following the principles of the *Guide to the Expression of Uncertainty in Measurement* (GUM) [6]. Miller *et al* [7] claimed an error estimate from emissivity of 4% at 200 °C to less than 1% above 550 °C using the emissivity uncertainty calculations developed by Madding [8]. Outeiro *et al* [9] claimed a total temperature error of less than 6% when using a charge-coupled device (CCD) camera sensitive to visible and near IR requiring relatively high temperatures (420 °C to 757 °C) and emissivity. For their thermography system measuring orthogonal cutting of 1045 steel tubes, Davies *et al* [10] provided an uncertainty statement of three components: calibration uncertainty, random experimental error and shift in emissivity value. They claimed a combined standard uncertainty of  $\pm 52$  °C for measured temperatures up to 850 °C, though many of the uncertainty sources later listed by Whittenton [1, 2] were neglected. Ivester [12] referenced Whittenton's work when reporting an expanded uncertainty of  $\pm 25$  °C (coverage factor  $k = 2$  [11]) for their measured maximum tool temperatures during orthogonal cutting of titanium alloy (Ti-6Al-4V). Since thermographic measurement uncertainties are generally difficult to discern, Arriola *et al* [13] took the approach of embedding thermocouples into the tool face and imaging the tool and thermocouple simultaneously. Thermography measurement of the thermocouple agreed well with the thermocouple value, though this procedure required very special tooling.

More information on thermographic measurement uncertainty is available from the radiation thermometry community. However, these works cover a broad range of applications that either neglect special considerations for metal cutting or focus on error sources that are negligible or non-existent in a metal cutting temperature measurement. Minkina and Dudzik [14, 15] describe the use of Monte Carlo simulations to determine uncertainty in thermographic temperature measurements. They state that analytical methods described in the GUM [6] cannot sufficiently account for all uncertainty sources due to the complicated nature of thermographic measurements. The Bureau International des Poids et Mesures (BIPM) Consultative Committee for Thermometry Working Group 5 (CCT-WG5) [16] provides uncertainty budgets for calibration of radiation thermometers below the ITS-90 silver point (961.78 °C) with meticulous analysis and references to many contributing works by its members. However, the CCT-WG5 document focuses on the calibration of single-point detectors and mentions that components of uncertainty incurred during measurements (subsequent to calibration) may dominate the total uncertainty depending on the nature of the measurement environment. As

mentioned in Davies *et al*'s review [4], this is very likely the case for metal cutting thermography, e.g. the uncertainty in emissivity of a measured object such as a cutting tool.

Few papers discuss the errors specific to a thermographic imaging system or detector array as opposed to a single-point thermometric system. More often, the detector array is assumed to act as a single detector without spatially varying sensitivity or effects from an imperfect optical system. Minkina and Dudzik [15] discussed PSF briefly, but did not add it as an uncertainty term in their numerical simulation. Three terms mentioned by Whittenton [1, 2], namely size of source effects, motion blur and PSF, substantially affect IR thermography of metal cutting by attenuating the maximum tool temperature measurement. Part of this attenuation can be accounted for by deconvolving a measured PSF [17]. However, uncertainty in the PSF introduces additional uncertainty in the tool temperature. While discussions of convolution procedures can be found in the literature, determination of propagated uncertainty of a deconvolved thermography image stemming from an uncertain PSF measurement is not covered.

In this paper, the measurand is the true maximum temperature of the side face of a cutting tool imaged by an IR thermal camera during the orthogonal cutting process. The maximum temperature  $T$  depends on governing variables  $x_i$  through some functional relationship  $T = f(x_1, x_2, \dots, x_N)$ . The *combined standard uncertainty*,  $u_c(T)$ , of the maximum temperature is determined through the law of propagation of uncertainty in the absence of variable correlations [6, 11]:

$$u_c^2(T) = u_{\text{cal}}^2(T) + \sum_{i=1}^N \left( \frac{df}{dx_i} \right)^2 u^2(x_i). \quad (1)$$

Each variable  $x_i$  of the measurement function  $f$  (detailed in section 2) has its own associated *standard uncertainty of the variable*  $u(x_i)$  that contributes to the overall combined standard uncertainty  $u_c$  as shown in equation (1). In this paper, the sensitivity coefficients  $K_i = \partial f / \partial x_i$  are written as positive or negative to highlight the direction in which the variable tends to influence the measurement. Nomenclature for the component of standard uncertainty  $u_i(T)$  (also referred to as the standard uncertainty due to variable  $i$ ) is the product of the sensitivity coefficient  $K_i$  and the standard uncertainty  $u(x_i)$  of the variable  $x_i$ . Standard uncertainty of the variable is determined either through type-A or type-B analyses. Equation (1) neglects correlation between governing variables. Discussion of potential correlation and its contribution to the combined uncertainty is given at the end of this paper.

Some components of the measurement uncertainty may be determined analytically using an approach outlined in the GUM. Others, in particular effects that depend on a pixel's neighbouring values, are quite complicated in nature and do not lend themselves to simple analytical methods, but may be determined through a numerical Monte Carlo approach. This paper demonstrates both methods and outlines the procedure(s) to determine the measurement uncertainty applicable to other similar IR thermographic measurements.

## 2. The measurement process chain

Every IR thermography measurement includes an emitting source of radiation and a detector with related output signal. As noted by DeWitt and Nutter [18], temperature cannot be directly measured through radiometric or thermographic methods, but may only be inferred from the detector signal, which is directly related to the incident radiation flux. However, the detector incident flux is not solely from a single emitting source and is most often contaminated by extraneous flux sources of varying degree. A physics-based model (measurement equation) is required to relate radiation flux from the source whose temperature is to be measured to the flux incident on the detector and the resulting signal. This is combined with a detector calibration function that relates signal to temperature of a pure blackbody source. Variables used in the measurement equation and calibration function are required inputs, and have some uncertainty about their nominal or measured values.

### 2.1. The physical model

Planck's law gives the spectral radiance of a blackbody source  $L_{\lambda,b}$ , at temperature  $T$ , in units of power emitted per surface area per wavelength per solid angle ( $\text{W m}^{-3} \text{sr}^{-1}$ ) for  $T$  given in units of K:

$$L_{\lambda,b}(T) = \frac{c_{1L}}{\lambda^5 [\exp(c_2/\lambda T) - 1]} \quad (2)$$

where  $c_{1L} = 1.1910439 \times 10^{-16} \text{ W m}^2$  and  $c_2 = 0.014388 \text{ m K}$  are constants [18, 19]. The power per unit wavelength, or *spectral radiant flux* (also called *spectral power*),  $\Phi_\lambda$  (units of  $\text{W m}^{-1}$ ) collected by the optics, from an object scenel of area  $A$ , is approximated by the following:

$$\Phi_\lambda(T) \approx \Omega A L_{\lambda,b}(T) \quad (3)$$

where  $\Omega$  is the solid angle formed between the pixel and optics aperture. The approximate equal sign ( $\approx$ ) is used here since  $\Phi_\lambda$  is in reality scaled by some spectral object emissivity,  $\varepsilon_\lambda$ . For opaque objects, the reflectivity of the surface is equal to  $1 - \varepsilon_\lambda$ , thus the scenel also reflects ambient radiation incident upon it. In a real system, the FPA or sensor will not collect the entire radiation emitted from the source, but an amount attenuated by transmission through the environment and optics. Minkina and Dudzik investigated measurement uncertainty associated with multiple extraneous flux sources from ambient surroundings, the air and the optics [15]. For microscopic IR thermographic measurement over short distances, the transmission band of the optics, typically determined by a bandpass filter, can be chosen to not include strong atmospheric absorption lines, so that emission from and transmission loss through the air may be neglected. In addition, measurement of small heat sources, exposure of the optics to the heat source for short durations of the measurement, and the use of temperature-controlled optics cause the optics temperature to remain near or below the ambient temperature ( $T_{\text{amb}}$ ), and thus emission from the optics may be assumed to be part of the flux from ambient sources or negligible. Effects due to emission from and transmission

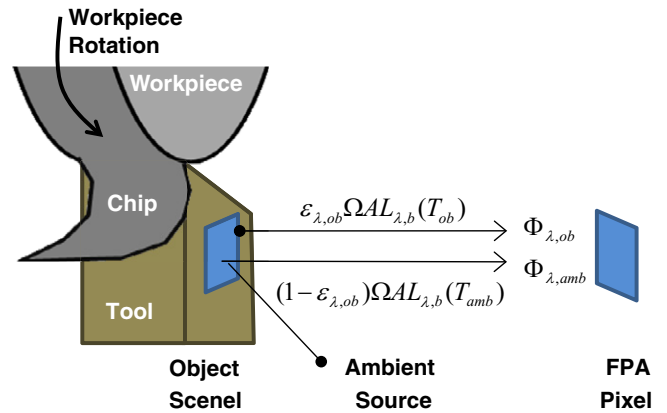


**Figure 1.** Schematic showing simplified version of flux components on the FPA used in the measurement equation [1, 2, 7, 16, 20].

through the air and optics may also be ignored if they are assumed constant through each step of the calibration and measurement process. This is especially true in the case where the filter is a cold filter, so that changes in the temperature of the filter, as well as the radiation emitted by it, are negligible. Figure 1 shows the schematic representing the orthogonal cutting tests performed at NIST. The spectral measurement equation corresponding to this measurement setup is given by

$$\Phi_\lambda(\varepsilon_\lambda, T_s, T_{\text{amb}}) = \Omega A [\varepsilon_\lambda L_{\lambda,b}(T_{\text{ob}}) + (1 - \varepsilon_\lambda) L_{\lambda,b}(T_{\text{amb}})]$$

$$S(\varepsilon_\lambda, T_s, T_{\text{amb}}) = \alpha \cdot \int_{\lambda_1}^{\lambda_2} w_\lambda \cdot \Phi_\lambda d\lambda. \quad (4)$$

Here,  $w_\lambda$  is the spectral responsivity of the camera and the integration limits coincide with the transmission band of the optics.  $T_{\text{ob}}$  is the temperature of the measured object scenel. For a camera with linear response,  $\alpha$  is a scale factor for conversion of the flux incident on a pixel into signal and is dependent on the sensor, readout electronics, integration time, etc.

Equation (4) is further simplified by the following assumptions: (1) emissivity is not temperature dependent over the measured range<sup>3</sup>, (2) emissivity does not vary with wavelength over the bandpass of the system and (3) if the camera were measuring a pure blackbody source of  $\varepsilon = 1$ , there is a function  $S_b(T)$  that relates the signal  $S$  to the blackbody temperature. When applied to equation (4), these assumptions yield the *non-spectral measurement equation*.

$$S(\varepsilon, T_{\text{ob}}, T_{\text{amb}}) = \varepsilon \cdot S_b(T_{\text{ob}}) + (1 - \varepsilon) \cdot S_b(T_{\text{amb}}). \quad (5)$$

The measurement equation (5) can be used to infer the object scenel temperature  $T_{\text{ob}}$  if  $\varepsilon$ ,  $T_{\text{amb}}$  and  $S_b$  are known.

### 2.2. Calibration function

In order to determine  $S_b(T)$ , the function relating the blackbody source temperature to the signal, a *blackbody calibration* is performed. This is done by focusing the camera at the aperture of a variable temperature blackbody source with

<sup>3</sup> This is a material and/or process-dependent assumption. For example, in IR thermographic measurement of cutting tools, high temperatures may oxidize the tool surface during cutting, which effectively raises the emissivity.

a real emissivity very close to 1 and measuring the signal at different temperatures spanning the range of interest. This is followed by a curve fitting process to determine a *calibration function*  $F$ , which approximates the actual signal measured,  $S$ :

$$S \approx S_b(T_b) \approx F(T). \tag{6}$$

The left approximation sign shows how equations (4) and (5) are reduced for a blackbody source of emissivity very close to 1. The right approximation sign states that the relationship between the output signal  $S$  and the calibration blackbody temperature  $T_b$  is approximated by the calibration function  $F$ . The calibration function may be defined using polynomial, spline or other analytical functions (e.g. Sakuma–Hattori equation [21]), or a lookup table. Its overall purpose is to convert between a signal and an equivalent, hypothetical perfect blackbody temperature called the apparent temperature,  $T_{app}$ . With this definition, the calibration equation (6) and measurement equation (5) may form the *combined measurement equation*:

$$S = F(T_{app}) = \varepsilon \cdot F(T_{true}) + (1 - \varepsilon) \cdot F(T_{amb}). \tag{7}$$

Given a measured signal  $S$  and  $F$  known from calibration,  $F$  may be inverted to solve for apparent temperature  $T_{app} = F^{-1}(S)$ . During blackbody calibration at high temperatures,  $T_{app}$  is usually taken to be equal to the calibration blackbody temperature because the emissivity is very close to one and the blackbody emits orders of magnitude more radiation than the ambient ( $F(T_{true}) \gg F(T_{amb})$ ). Radiation thermometers and cameras often output  $T_{app}$  using an internally stored calibration function  $F$  rather than or in addition to signal values (digital levels (DLs) or counts). These internal calibrations may or may not use a measurement equation similar to equation (5) with user inputs for  $\varepsilon$  and  $T_{amb}$ .

Once the blackbody calibration is completed, and the emissivity of the measured object is known, it is possible to calculate a *true object temperature*  $T_{true}$  from a measurement. This is done by solving for  $T_{true}$  in equation (7):

$$T_{true} = F^{-1} \left[ \frac{F(T_{app})}{\varepsilon} - \frac{(1 - \varepsilon)}{\varepsilon} \cdot F(T_{amb}) \right]. \tag{8}$$

### 2.3. Example calibration functions and measurement equations

Measurement equations, calibration functions and their particular use depend on the application, user preferences and available outputs from the camera and frame grabber software. Outeiro *et al* used a measurement equation with the same components as equation (7) to correct their measurements for ambient reflection [9]. Rather than substituting their calibration function  $F(T)$ , they used the Stefan–Boltzmann law, which assumes that the sensor signal is proportional to  $T^4$ , and is only valid for spectral responsivities with a very large bandwidth. Handheld IR thermometers often include an internal calibration function that uses the detector body temperature to calculate the extraneous flux, and an emissivity setting intended to match the emissivity of the

measured object [22, 23]. Through the use of the measurement equation, a perfectly matched instrument emissivity setting will cancel the error associated with object emissivity. Often with thermal cameras intended to measure over a long distance, a measurement equation is used, which corrects for air transmission and emission terms [15, 24, 25].

Two example calibration/measurement methods using user-determined (external) and internally stored calibrations are described next. The first is a function called the Sakuma–Hattori equation used in external calibration. This is the basis for the analytical method for the measurement uncertainty given in section 3. The second method, using the internal camera calibration, is used in the numerical uncertainty analysis given in section 5.

2.3.1. *Sakuma–Hattori equation.* The most popular calibration function used in recent literature is the *Sakuma–Hattori equation* [10, 21, 22, 26–28]. This equation closely approximates Planck’s law integrated over spectral responsivity, and can be easily inverted. The Planckian form of the Sakuma–Hattori equation is given by

$$F(T) = \frac{C}{\exp\left(\frac{c_2}{AT + B}\right) - 1}. \tag{9}$$

Here,  $c_2$  is the second radiation constant defined in equation (2), and  $A$ ,  $B$  and  $C$  are constants determined through least-squares curve fitting to signal and temperature data from a blackbody calibration. The denominator in the argument of the exponential is often written as  $\lambda_x \cdot T$ , where  $\lambda_x$  is the temperature-dependent extended effective wavelength [29]. In multiple references using the Sakuma–Hattori equation,  $\lambda_x$  is assumed to be  $\lambda_x = A + B/T$  [16, 23, 27–29].

The physical relationship between the coefficients  $A$ ,  $B$  and  $C$  and the system spectral responsivity is given by Saunders in terms of central wavelength,  $\lambda_0$ , and the standard deviation of wavelengths in the band,  $\sigma$ , for systems with narrow-band spectral responsivities as [27]

$$\begin{aligned} A &\approx \lambda_0 \cdot \left( 1 - 6 \cdot \left( \frac{\sigma}{\lambda_0} \right)^2 \right) \\ B &\approx \frac{c_2}{2} \cdot \left( \frac{\sigma}{\lambda_0} \right)^2 \\ C &= \int_0^\infty \frac{w_\lambda}{\lambda^5} d\lambda \approx \frac{a}{\lambda_0^5}. \end{aligned} \tag{10}$$

Substituting equation (10) into (9), then into (7) gives a combined measurement equation in terms of camera responsivity parameters that is apt for analytical uncertainty evaluation in section 3 similar to the methods provided in the ASTM International standard (ASTM E2847-11) [22].

2.3.2. *Radiance-based measurement equation with internal camera calibration.* Another method for determining the true object temperature is to use the internal calibration function (obtained from a blackbody calibration) stored in the camera

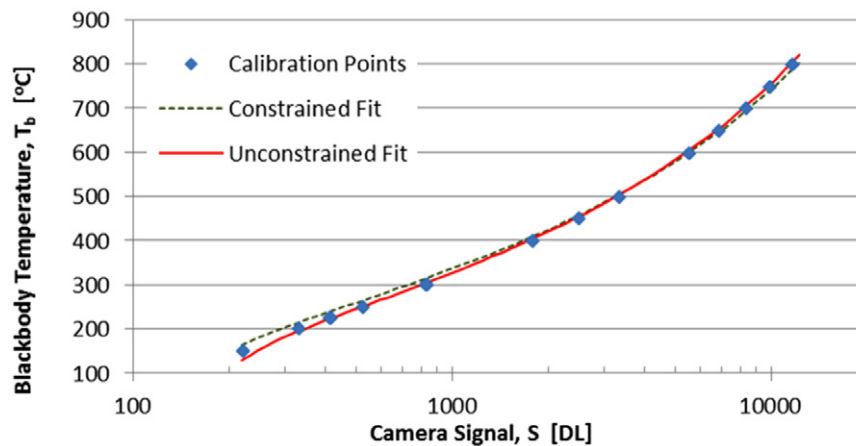


**Figure 2.** Blackbody calibration data for the COTS camera fitted to the Sakuma–Hattori equation.

to convert a signal to apparent temperature. It is particularly useful for handling wide-band spectral responsivities  $w_\lambda$  or spectrally dependent object emissivity. To determine the true object temperature  $T_{\text{true}}$  from the camera output  $T_{\text{app}}$ , one must use the inverted measurement equation similar to equation (7). However, in this case,  $F$  is unknown since it is internal to the camera. For the purpose of converting  $T_{\text{app}}$  to  $T_{\text{true}}$ , the assumption is made that  $F(T)$ , which relates the total signal to an apparent blackbody temperature, can be obtained using equation (4):

$$F(T_{\text{app}}) = \alpha \cdot \int_{\lambda_1}^{\lambda_2} w_\lambda L_{\lambda,b}(T_{\text{app}}) d\lambda. \quad (11)$$

Note that the real relationship between signal and an apparent blackbody temperature is internal to the camera and this equation is a physics-based tool to approximate the calibration function for conversion of  $T_{\text{app}}$  to  $T_{\text{true}}$ . In application, substituting equation (11) into the left-hand side of equation (4), and cancelling the scaling constant  $\alpha$ , yields the following measurement equation:

$$\begin{aligned} & \int_{\lambda_1}^{\lambda_2} \frac{w_\lambda}{\lambda^5} \left[ \frac{1}{\exp(c_2/\lambda T_{\text{app}}) - 1} \right] d\lambda \\ &= \int_{\lambda_1}^{\lambda_2} \frac{w_\lambda}{\lambda^5} \left[ \frac{\varepsilon_{\text{ob},\lambda}}{\exp(c_2/\lambda T_{\text{true}}) - 1} \right. \\ & \quad \left. + \frac{1 - \varepsilon_{\text{ob},\lambda}}{\exp(c_2/\lambda T_{\text{amb}}) - 1} \right] d\lambda. \end{aligned} \quad (12)$$

Since this combined measurement equation is in integral form, one cannot explicitly solve for  $T_{\text{true}}$ . If discrete vectors  $w_\lambda$ ,  $\varepsilon_{\text{ob},\lambda}$  and  $\lambda$  are known, given  $T_{\text{app}}$  and  $T_{\text{amb}}$ ,  $T_{\text{true}}$  can be solved numerically by moving the  $T_{\text{app}}$  component to the right of the equal sign in equation (12), and treating the resulting equation as a minimization problem.

### 3. Analytical method for measurement uncertainty of independent sensors

This section gives an analytical approach for determining measurement uncertainty components for each independent

sensor in an array. Phenomena such as optical and motion blurring, pixel crosstalk, etc, cause a given pixel's values to be affected by neighbouring pixel values. This is not easily handled by the analytical method in this section since these effects are dependent on the particular imaged scene. Therefore, they are addressed through numerical analysis using an example scene in the next section.

Building on the combined measurement equation (equation (7)), the true maximum temperature (measurand) is described in terms of the variables  $x_i$ , allowing sensitivity coefficients  $K_i$  to be calculated according to the propagation of uncertainty in equation (1). First, the uncertainty component due to calibration is described, which also presents the nominal values for system responsivity central wavelength,  $\lambda_0$ , and standard deviation of wavelengths in the band,  $\sigma$ . The other uncertainty components, due to uncertainty in responsivity, uncertainty in emissivity and uncertainty in ambient temperature, are then discussed.

#### 3.1. Uncertainty due to calibration curve fitting

Uncertainty in calibration arises from uncertainty in the temperature of the blackbody and uncertainty caused by approximating the actual response using a calibration function. The uncertainty in the blackbody temperature is usually small if it is calibrated.

The real spectral responsivity of the COTS camera is known to be governed by the bandwidth of the narrow-band filter, which has a uniform bandpass between  $\lambda_l = 3.79 \mu\text{m}$  and  $\lambda_r = 4.06 \mu\text{m}$ . This gives a central wavelength of  $\lambda_0 = (\lambda_r + \lambda_l)/2 = 3.925 \mu\text{m}$ . The standard deviation of the uniform distribution is given by  $\sigma = (\lambda_r - \lambda_l)/\sqrt{12} = 0.061 \mu\text{m}$ . Since these values are known, equation (10) is used to derive the Sakuma–Hattori coefficients  $A$  and  $B$ . This leaves the coefficient  $C$ , or  $a$  in equation (10), to be determined by least-squares approximation. Figure 2 shows that a good fit to the COTS camera calibration data is obtained by using the inverse Sakuma–Hattori equation to fit the temperatures estimated based on the measured signal to the actual temperature of the blackbody. Since the low and high temperatures are of the same order of magnitude, while the low and high values of intensity

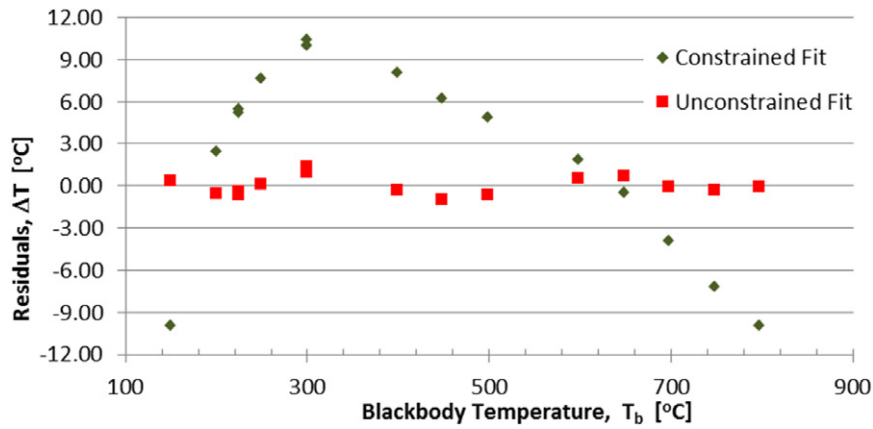


**Figure 3.** Residual errors from the Sakuma–Hattori calibration fit for the constrained fit (coefficients  $A$  and  $B$  are set based on the system spectral response) and the unconstrained fit.

differ by nearly three orders of magnitude, the inverse fit is a simple way to weight the data points evenly.

This curve fit for the constrained curve in figure 2 resulted in the following Sakuma–Hattori coefficients:  $A = 3.9166 \mu\text{m}$ ,  $B = 1.7816 \mu\text{m K}$  and  $C = 3.570 \times 10^5$  (resulting in  $a = 3.33 \times 10^8$ ). The unconstrained fit gave  $A = 4.0879 \mu\text{m}$ ,  $B = 0.3870 \mu\text{m K}$  and  $C = 2.907 \times 10^5$ . Both fits used a radiation constant  $c_2 = 14\,388 \mu\text{m K}$ . The residual errors  $\Delta T_i = F^{-1}(S_i) - T_b$ , shown in figure 3, are the difference between the temperature estimated from the inverse Sakuma–Hattori curve fit and the actual blackbody temperature. This shows that curve fitting while constraining  $A$  and  $B$  to values expected for known filter characteristics results in residuals up to  $10^\circ\text{C}$ , which also show a systematic pattern. Curve fitting without these constraints results in residuals less than  $1.4^\circ\text{C}$ , and without any systematic trend.

Although error in calibration depends on the temperature, a single value for the standard uncertainty due to calibration,  $u_{\text{cal}}$ , is given by the *standard error of estimate*, which is the standard deviation of all the residual errors. The standard error of estimate for all  $\Delta T_i$  in figure 3 is  $u_{\text{cal}} = 0.67^\circ\text{C}$  for the unconstrained fit and  $6.9^\circ\text{C}$  for the constrained fit.

In reality, the COTS camera uses an internal, piece-wise linear calibration function rather than a least-squares fit to the Sakuma–Hattori equation [25]. It also internally compensates for camera body temperature, which causes slight effects on the camera responsivity (the fits above used only the calibration data obtained with camera body temperatures between  $28^\circ\text{C}$  and  $30.5^\circ\text{C}$ ). Since this internal calibration is expected to be more accurate than the Sakuma–Hattori fit, the  $u_{\text{cal}}$  value, determined above for the unconstrained fit, is a conservative estimate.

### 3.2. Measurement equation and sensitivity coefficients

The use of equation (10) to describe the calibration coefficients allows the investigation of the measurement uncertainty due to uncertainty in spectral responsivity,  $u(\lambda_0)$ . Substituting the responsivity relationships in equation (10) into the Sakuma–Hattori equation (equation (9)) gives the following form of the

non-spectral measurement equation:

$$F(T) = \frac{a}{\lambda_0^5} \left[ \exp \left( \frac{c_2 \lambda_0^2}{\lambda_0^3 T - 6 \lambda_0 T^2 \sigma^2 + 1/2 c_2 \sigma^2} \right) - 1 \right]^{-1}$$

$$S = F(T_{\text{app}}) = \varepsilon \cdot F(T_{\text{true}}) + (1 - \varepsilon) \cdot F(T_{\text{amb}}). \quad (13)$$

One way to determine the uncertainty of  $T_{\text{true}}$  is to explicitly solve for it using equation (13) and take the partial derivatives with respect to variables,  $x_i$ . The sensitivity coefficients may also be determined by implicit differentiation. This method is used in ASTM E2847-11 [22] and yields

$$K_i = \frac{\partial T_{\text{true}}}{\partial x_i} = \frac{\partial S}{\partial x_i} \cdot \left( \frac{\partial S}{\partial T_{\text{true}}} \right)^{-1}$$

$$= \frac{\partial F(T_{\text{app}})}{\partial x_i} \cdot \left( \frac{\partial F(T_{\text{app}})}{\partial T_{\text{true}}} \right)^{-1}. \quad (14)$$

Since  $a$  is a scaling parameter, it is cancelled essentially from both sides of the equation. While a shift in the central wavelength  $\lambda_0$  is possible due to filter axis tilt, temperature changes, etc, it is unlikely that the responsivity bandwidth  $\sigma$  can change significantly. Therefore, only the variables  $\lambda_0$ ,  $\varepsilon$  and  $T_{\text{amb}}$  are analysed for their sensitivity coefficients  $K_\lambda$ ,  $K_\varepsilon$  and  $K_{\text{amb}}$ , respectively.

Sensitivity to a shift in central wavelength is usually not of concern when a single narrow-band filter is being used. In the calibration process above, it was noted that constraining  $A$  and  $B$  to values dictated by the specified central wavelength and bandpass of the filter did not give as good a fit to the blackbody calibration data as an unconstrained fit, which indicated a different central wavelength. For this reason, the sensitivity to a shift in central wavelength of the filter is also being studied. However, it should be noted that if there is no scope for the central wavelength or other parameters of the calibration function to change between calibration and measurement, they will not lead to any uncertainty over and above the calibration uncertainty.

### 3.3. Calculated sensitivity coefficients and error

The expressions for the sensitivity coefficients  $K_i$  given in equation (14) are solved symbolically using commercial

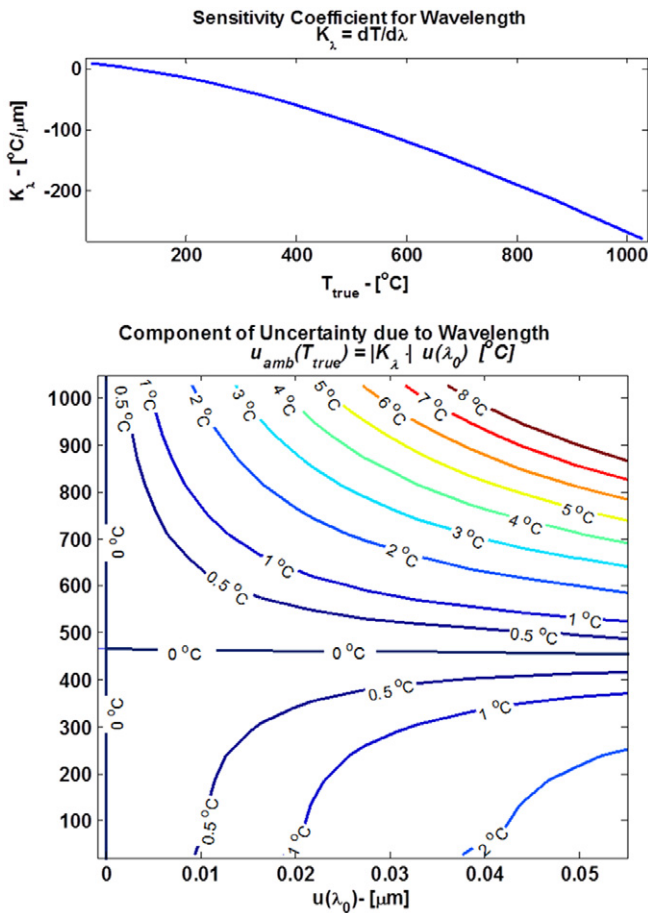


**Figure 4.** Temperature-dependent sensitivity coefficient (top) and component of standard uncertainty (bottom) due to uncertainty in the central wavelength of the camera spectral responsivity:  $\varepsilon = 0.8$ ,  $T_{\text{amb}} = 20^{\circ}\text{C}$  and nominal  $\lambda_0 = 3.9\mu\text{m}$ .

computer algebra software. These coefficients depend on the true temperature of the object being measured  $T_{\text{true}}$ , and on the other variables  $\lambda_0$ ,  $\varepsilon$  and  $T_{\text{amb}}$ . The  $K_i$  values are evaluated at nominal values of their corresponding variable. Uncertainty components are calculated as  $u_i(T_{\text{true}}) = K_i \cdot u(x_i)$ . To summarize the results, the calculated sensitivity coefficients  $K_i$  and the relevant components of standard uncertainty  $u_i(T_{\text{true}})$  for variable  $x_i$  are represented as contour plots using the uncertainty  $u(x_i)$  and true object temperature  $T_{\text{true}}$  as independent axes.

Nominal values for  $\lambda_0$ ,  $\varepsilon$  or  $T_{\text{amb}}$  are specific for the COTS camera used in this study. Figure 4 gives the coefficient  $K_\lambda$ , and associated component of standard uncertainty  $u_\lambda(T_{\text{true}})$  corresponding to an error in central wavelength  $u(\lambda_0)$ . A value of  $u(\lambda_0) = 0$  on the x-axis of the bottom plot in figure 4 corresponds to no uncertainty in  $\lambda_0$ .

The vertical  $0^{\circ}\text{C}$  contour at  $u(\lambda_0) = 0$  represents the fact that, if the uncertainty in  $\lambda_0$  is zero, the corresponding component of uncertainty in  $T_{\text{true}}$  is also zero for all measured  $T_{\text{true}}$ . The horizontal  $0^{\circ}\text{C}$  contour corresponds to the maximum of Planck's curve for a given wavelength  $\lambda_0$ , which occurs at a temperature of  $465.1^{\circ}\text{C}$  (given by Wien's displacement law [18]). The sensitivity is zero at this temperature because the derivative of Planck's curve with respect to the wavelength at that temperature is zero. In a similar manner, figure 5 gives

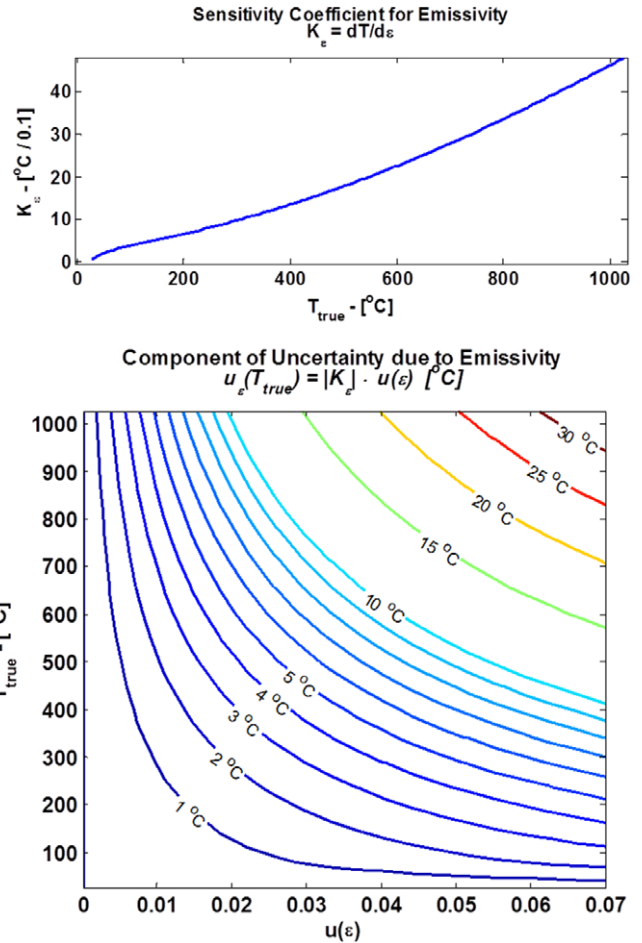


**Figure 5.** Temperature-dependent sensitivity coefficient (top) and component of standard uncertainty (bottom) due to uncertainty in measured object emissivity:  $\lambda_0 = 3.9\mu\text{m}$ ,  $T_{\text{amb}} = 20^{\circ}\text{C}$  and nominal  $\varepsilon = 0.8$ .

the result  $u_\varepsilon(T_{\text{true}})$  corresponding to an error in measured object emissivity  $u(\varepsilon)$ . Since  $\varepsilon$  is only defined between 0 and 1, the coefficient  $K_\varepsilon$  is given in units of  $^{\circ}\text{C}/0.1$ , corresponding to a change in  $T_{\text{true}}$  in  $^{\circ}\text{C}$  per change in  $\varepsilon$  of 0.1.

In metal cutting, it is common for hot chips in the vicinity of the tool to cause a higher  $T_{\text{amb}}$  that gets reflected by the surface being measured. The higher the temperature and volume of chips, and the lower the emissivity of the tool surface, the higher the effect of ambient temperature reflection. Figure 6 shows the component of measurement uncertainty due to uncertainty in ambient reflected temperature, for a surface with a nominal emissivity of 0.8.

When measuring an object at low temperatures near  $T_{\text{true}} = T_{\text{amb}} = 20^{\circ}\text{C}$ , figure 6 (top) shows that an uncertainty in  $T_{\text{amb}}$  has a greater effect on the measurement uncertainty. At higher measured temperatures, the measurement is much less sensitive to the error in ambient reflected temperatures.

Nominal values for each variable were set based on the use of the specific COTS camera configuration and cutting tools used in this study. However, it is likely that other systems with different spectral responsivities and measured object emissivities will result in similar shapes of the resulting contour plots for the sensitivity coefficients and components.

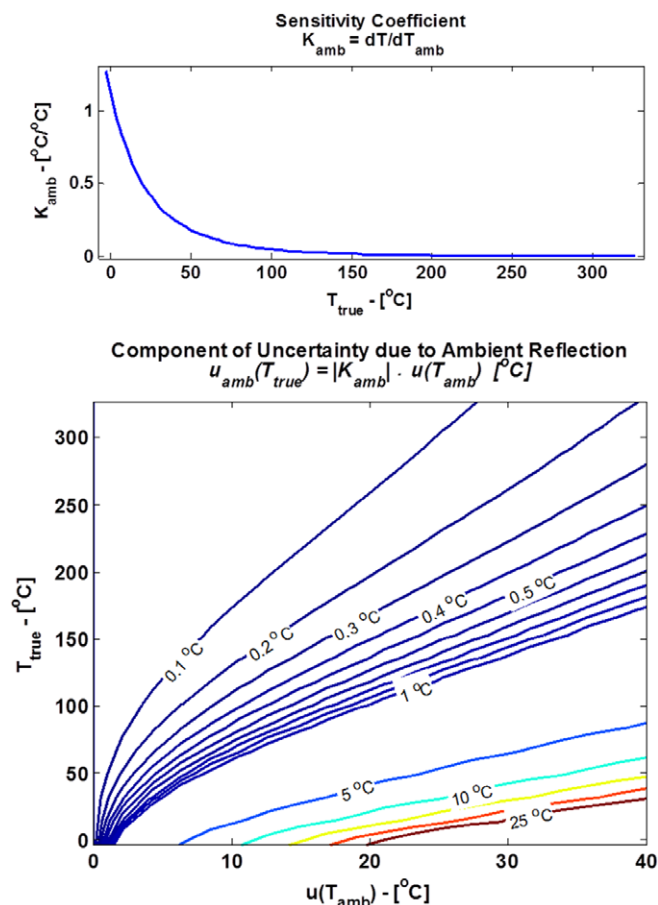


**Figure 6.** Temperature-dependent sensitivity coefficient (top) and component of standard uncertainty (bottom) due to uncertainty in the ambient reflected temperature (right):  $\epsilon = 0.8$ ,  $\lambda_0 = 3.9 \mu m$  and nominal  $T_{amb} = 20^{\circ}C$ .

These results apply to each detector in a FPA, and highlight the complex relation between each variable and its uncertainty component.

#### 4. Numerical study of uncertainties including the effect of convolution in sensor arrays

Sensors often contain only a single sensing element and yield a single measurement value. In contrast, an IR thermal camera uses a 2D FPA to measure an array of intensity values representing the IR radiation emitted by a 2D array of scenels on the measured surface. Both the optics and electronics of any camera system can introduce uncertainties in the images produced. This section describes the most significant uncertainty sources, setting the stage to use the Monte Carlo method to determine their magnitudes in the next section. While it is possible to determine such uncertainties analytically, the resulting uncertainty statement is often difficult to use in practice. For example, it may be possible to relate the temperature uncertainty to the spatial frequencies present in the thermal image and the motion and optical blurring. The Monte Carlo simulation using a ‘typical’ thermal image is a simpler way to estimate the relative magnitude of these uncertainties. In addition, it can verify some of the uncertainties determined analytically in section 3.

*Optical crosstalk* arises from unwanted diffraction, scattering and reflections in the imaging system, which causes the radiance of more than one scenel to affect the intensity value of a pixel. Even with a perfect optical system, relative motion between the camera and the surface being measured can lead to the radiance of many scenels contributing to a pixel’s value. *Electronic crosstalk* arises when the construction of the electrical circuitry within the FPA causes intensity values of some pixels to affect the intensity values of other pixels. Both optical crosstalk and electronic crosstalk are especially noticeable when there is a high ratio between the intensities of the brightest and darkest areas of an image.

*Optical resolution* is determined primarily by the way light interacts with the optical system of the camera. Optical resolution is not accurately described by a single number, but functions such as a PSF. There are several techniques available for measuring such functions [30–32]. One way of thinking of a PSF is to imagine the camera focused on a point source of light incident at the centre of one pixel of the FPA. If there were no optical or electronic crosstalk, the FPA would report one bright pixel, with all neighbouring pixels having an intensity value of 0. Unfortunately, even when the image is in focus, real optics spread this point over an area. The function describing how the light is spread is the PSF corresponding to that pixel of the image. The PSF is almost always assumed to be radially symmetric and of equal magnitude at every location in the image, though this is not always the case. In diffraction-limited optics, the wavelength of light limits the optical resolution; shorter wavelengths can resolve smaller features than longer wavelengths. *Size of source effect* refers to the fact that IR thermal cameras tend to underestimate temperature when measuring very small ‘hot spots’. A ‘hot spot’ is a group of one or more scenels that are similar in temperature and are significantly hotter than the surrounding scenels. The surrounding scenels are sometimes referred to as the ‘background’. Size of source effects arise from PSF and other causes of crosstalk among pixel values when the hot spot is larger than a scenel, and from averaging when the hot spot is smaller than a scenel.

The size of source effect arising when the source is smaller than a scenel is illustrated in figure 7. 3D finite element method (FEM) simulation of orthogonal metal cutting was used to obtain the steady state distribution of temperature over the side faces of the chip and the tool, as shown in figure 7(b). Using this in conjunction with an assumed distribution of emissivity (figure 7(a)), a corresponding (high-resolution) apparent temperature image (figure 7(c)) can be calculated using equation (12). To simulate an apparent temperature image observed by a camera (figure 7(d)), the FEM-generated apparent temperature image is converted to an intensity image, is smoothed and resampled to match the scenel size and scenel spacing of the camera, and is then converted back into an apparent temperature image. Each pixel in the simulated camera image results from an averaged area (approximately 6 pixel by 6 pixel group) in the high-resolution image. Naturally, both maximum apparent temperatures in the tool and in the chip are lower in this camera resolution image, due to the averaging, which is the cause of the sub-pixel size of source

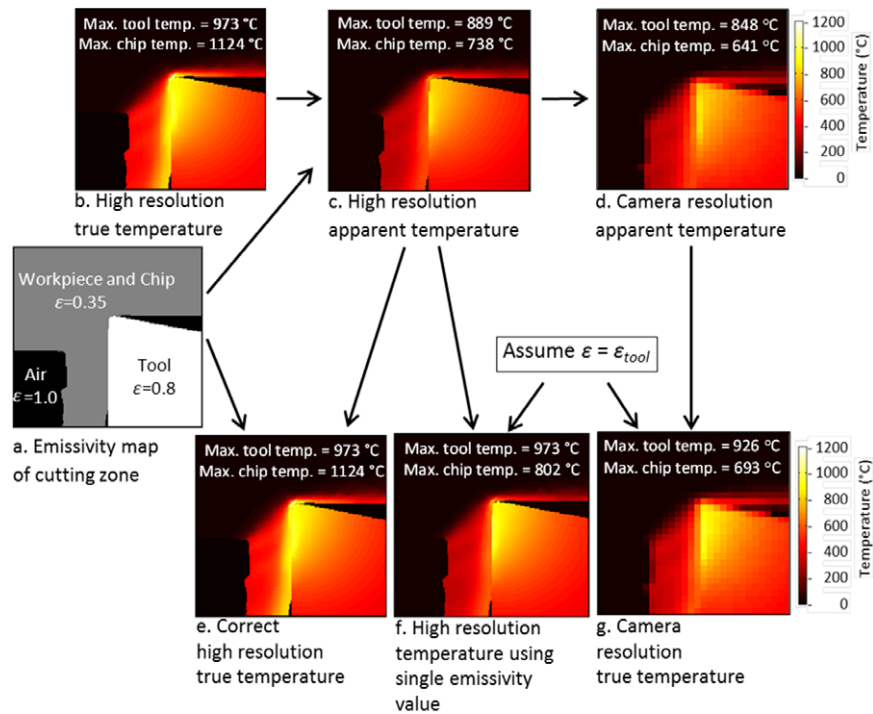


**Figure 7.** Effect of scenel size and emissivity on a ‘perfect’ (no PSF) camera. The field of view is 1 mm wide. High-resolution (FEM-generated) images are 6  $\mu\text{m}/\text{scenel}$ . Simulated camera resolution image is 37.5  $\mu\text{m}/\text{scenel}$ .

effect. This represents how a ‘perfect’ (no PSF) camera and optical arrangement, with scenel size larger than the hot spot, would image the scene. The fill factor (scenel size/scenel spacing) is assumed to be 1.

For the Monte Carlo simulation of the measurement process, once an apparent temperature image is acquired, it must be converted to true temperature. From the information in figures 7(a) and (c), the true temperature can be computed using equation (12), as shown in figure 7(e). In practice, precisely knowing the emissivity map is difficult, especially for the chip. Since we are ultimately trying to measure the tool temperature, it is expedient to simply use the emissivity of the tool for the entire image and compute the true temperature, in which case figure 7(f) is produced. As expected, the maximum computed true temperature for the chip is lower than the actual value, due to the use of the higher tool emissivity in the calculation. When the true temperature is computed beginning with the camera resolution image (figure 7(d)) using a constant emissivity equal to that of the tool, figure 7(g) is produced. Even the maximum calculated true temperature of the tool is lower than the true value due to the sub-pixel size of source error.

Comparing figure 7(d) with figure 7(c), a reduction in maximum apparent temperature can be observed as noted before. Figure 8 shows a zoomed view of the high-resolution image (figure 7(b)) obtained from FEM. The hottest tool temperatures in the high-resolution image are only a few pixels wide in the horizontal direction. Since the camera pixel size is  $\sim 6\times$  larger than the high-resolution image pixel, the size of the hot spots is smaller than a single pixel in the camera image, and the combination of the radiation emitted by the hot spot with that emitted by cooler regions around it results in

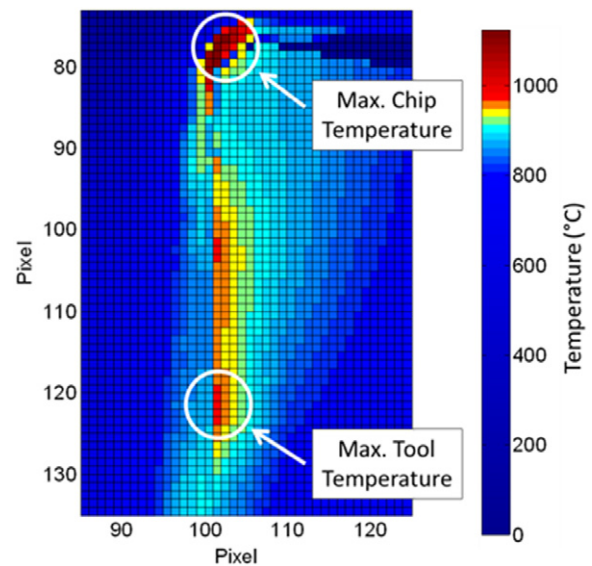


**Figure 8.** A magnified view of the region around the chip–tool interface in the high-resolution true temperature image. The maximum chip temperature occurs in a group of a few pixels near the cutting edge. The maximum tool temperature occurs in a thin strip of pixels along the rake face.

the sub-pixel size of source error. If only the camera image is available, this type of size of source error cannot be corrected unless assumptions are made about the size of the hot spot and the temperature distribution around it.

Size of source effects may also be seen even when the hot spot is several pixels in diameter. Figure 9 shows how the size of a hot spot affects the maximum single pixel temperature when the hot spot is larger than a pixel. It is modelled based

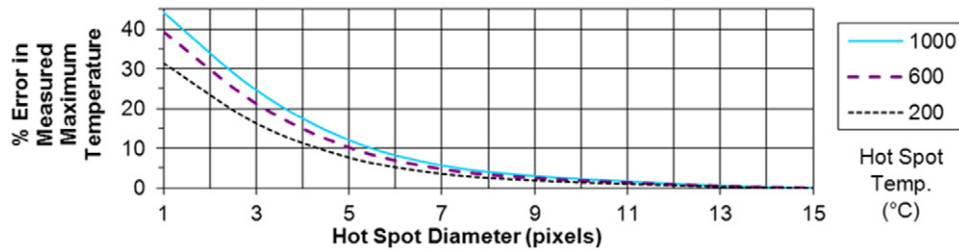


**Figure 9.** Percentage error in measured maximum single pixel temperature value at three hot spot true temperatures: 1000 °C, 600 °C and 200 °C. Error is defined in equation (15). The background is 100 °C and the ambient temperature is 20 °C.

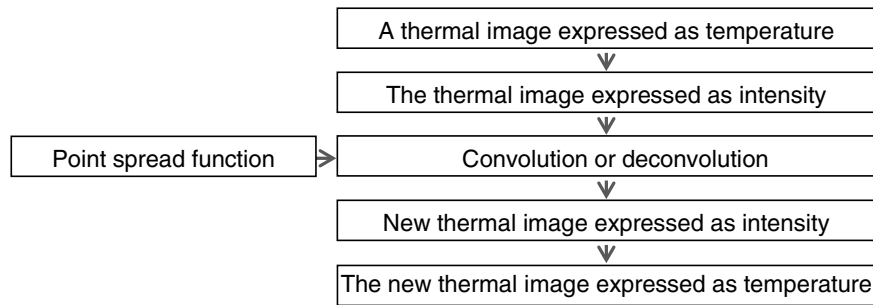


**Figure 10.** PSF is used to either simulate a camera image (using convolution) or correct a camera image (using deconvolution).

on the measured PSF of the COTS camera used in this study.

$$\%Error = 100\% \times \left| \frac{\text{Measured Temperature} - \text{True Temperature}}{\text{True Temperature}} \right| \quad (15)$$

When the size of the hot spot is at least a few pixels wide in the camera image, size of source error arising from the PSF of the optics may be simulated or corrected using convolution or deconvolution with the PSF, as shown in figure 10. In practice, deconvolution is more sensitive to noise than convolution. In this study, the Matlab function ‘deconvreg’ was used to perform deconvolution.

Figure 11 shows the effect of convolving the PSF with the COTS camera apparent temperature image following the steps in the flowchart in figure 10. The maximum apparent temperature within the tool decreases from 848 °C to 755 °C and edges in the image are smoothed.

### 5. Monte Carlo simulation method for uncertainty estimation

Monte Carlo simulation is used to determine sensitivity values used in estimation of the uncertainty in temperature measurement [17, 33]. Using Simpson’s rule to integrate equation (12), equation (16) is a minimization problem applied to each pixel. Given ambient temperature,  $T_{amb}$ , and vectors  $\lambda_i$ ,  $w_i$  and  $\varepsilon_i$ , this can be used to calculate the apparent temperature,  $T_{app}$ , given true temperature,  $T_{true}$ , or vice versa.  $\lambda_i$  is an  $N$  element vector defining the wavelengths to be used in the numerical integration. Each element in  $\lambda_i$  has an associated element in  $w_i$  quantifying the camera’s response at that wavelength and an associated element in  $\varepsilon_i$  quantifying the target’s emissivity at that wavelength. The narrow-band filter, which controls the overall system responsivity, has nearly

uniform transmissivity. So the weights,  $w_i$ , in equation (16) were assumed to be 1 for all  $\lambda_i$  spanning the bandpass of the filter. The  $\varepsilon_i$  were assigned either the value of the tool (0.8) or the workpiece (0.35) independent of wavelength.

$$\sum_{i=1}^N \frac{w_i}{\lambda_i^5} \left( \frac{1}{\exp(c_2/\lambda_i T_{app}) - 1} - \frac{\varepsilon_i}{\exp(c_2/\lambda_i T_{true}) - 1} - \frac{1 - \varepsilon_i}{\exp(c_2/\lambda_i T_{amb}) - 1} \right) \xrightarrow{\text{Minimize}} 0 \quad (16)$$

Equation (16), combined with the convolution/deconvolution technique in figure 10, and the FEM images shown in figures 7(a) and (b), was used to create a Monte Carlo simulation of the measurement process. The algorithm is shown in figure 12 and comprises the main steps of sampling the random variables, simulating a camera measurement of the true temperature field in figure 7(a) as influenced by the random variables, carrying out the data processing required to calculate the true temperature field from the camera measurement (similar to figure 7(g)), and calculating the error in maximum value of the actual true temperature field in figure 7(a) as compared with the measured true temperature field.

Estimated values  $\varepsilon_{tool}$ ,  $\lambda$ ,  $T_{amb}$  and  $PSF$  are used to process thermal camera images in practice.  $\varepsilon_{tool}$  is the emissivity of the tool.  $\lambda$  is the range of wavelengths of light imaged from 3.79  $\mu\text{m}$  to 4.06  $\mu\text{m}$ .  $T_{amb} = 20$  °C is the ambient temperature.  $PSF$  is a 15  $\times$  15 matrix representing the discretized form of the PSF for the pixel grid spacing shown in figure 12(b).  $Motion_x$  and  $Motion_y$  represent the horizontal and vertical motion of the camera relative to the imaged target (cutting tool) and are used only for simulating the camera measurement, but not for calculating the temperature field.  $\varepsilon_{chip}$  is the emissivity of the chip and workpiece, which is not used in temperature calculations.

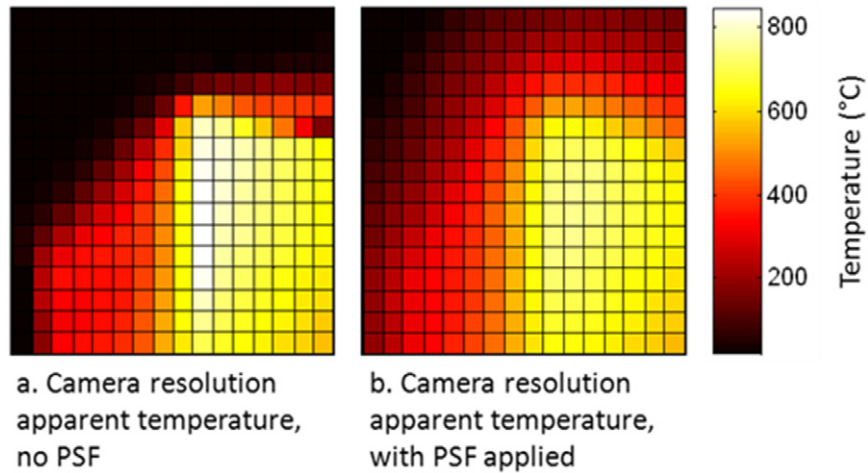


**Figure 11.** Effect of convolving the PSF with apparent temperature to produce a ‘measured’ image from the ‘perfect’ image.

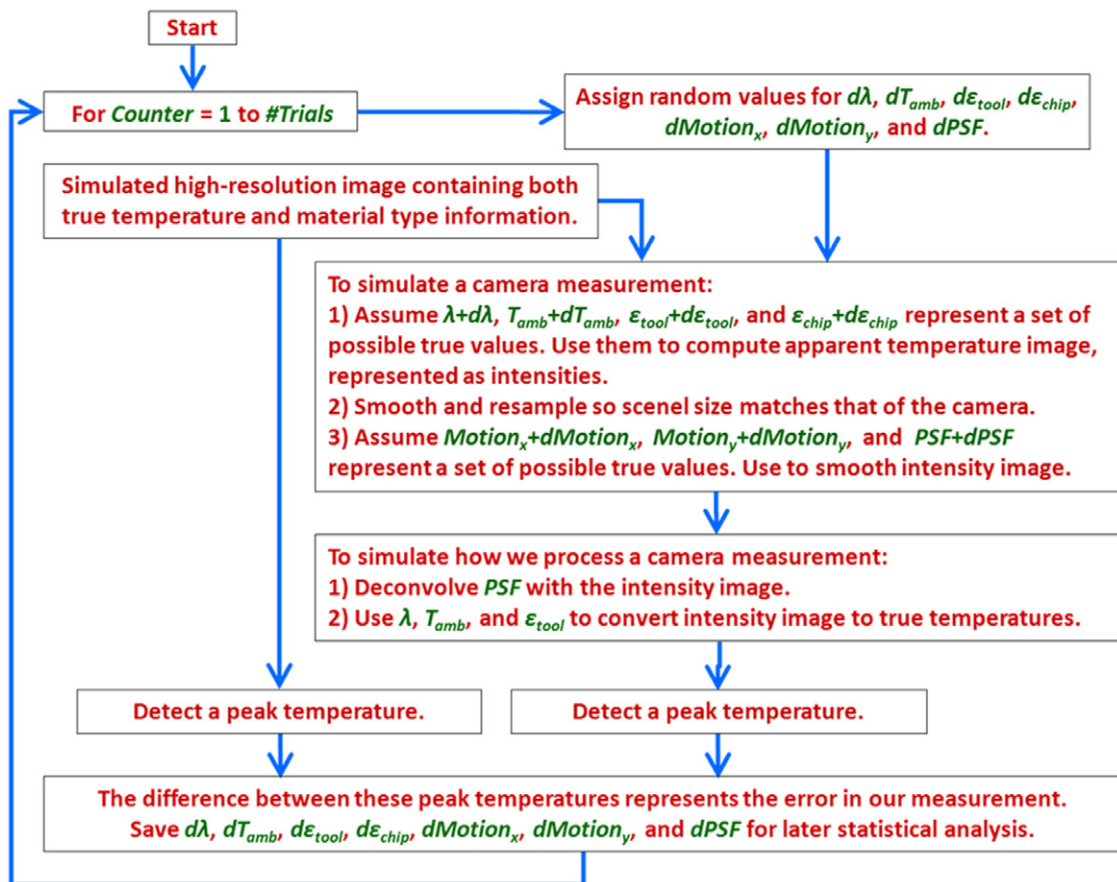


**Figure 12.** Simplified representation of Monte Carlo simulation. Statistical analysis of results will be used to determine uncertainties.

In the Monte Carlo simulations,  $\lambda$  is varied from  $3.79 \mu\text{m}$  to  $4.06 \mu\text{m}$ , over 101 uniform wavelength steps,  $d\lambda$ . The following nominal values for other variables are used:  $T_{\text{amb}} = 20^\circ\text{C}$ ,  $\varepsilon_{\text{tool}} = 0.8$ ,  $\varepsilon_{\text{chip}} = 0.35$ . Emissivity of the portions of the image representing air is assumed to be 1. Figure 13 shows the assumed distributions of the random variables for the Monte Carlo simulation, which are determined based on expected worst-case scenarios (type-B uncertainty estimate). A uniform distribution with a range of  $-0.025 \mu\text{m}$

to  $+0.025 \mu\text{m}$  is assumed for  $d\lambda$  to simulate the effect of the filter bandpass wavelength potentially shifting. A sample from the distribution,  $d\lambda$ , is added to every element of the vector  $\lambda_i$  to simulate shifting of the bandpass by  $d\lambda$ . A log-normal distribution is assumed for the  $dT_{\text{amb}}$  to simulate fluctuations in environment temperature, as well as radiation from hot chips reflecting off the cutting tool. The distribution for  $d\varepsilon_{\text{tool}}$  is estimated from measurements of the emissivity made while oxidizing the side faces of the tools. The software ensures

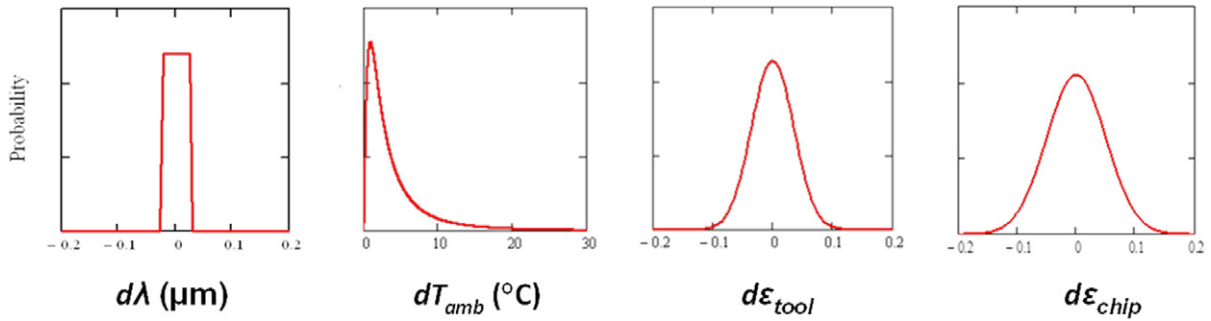


Figure 13. Probability distributions for  $d\lambda$ ,  $dT_{amb}$ ,  $d\epsilon_{tool}$  and  $d\epsilon_{chip}$ .

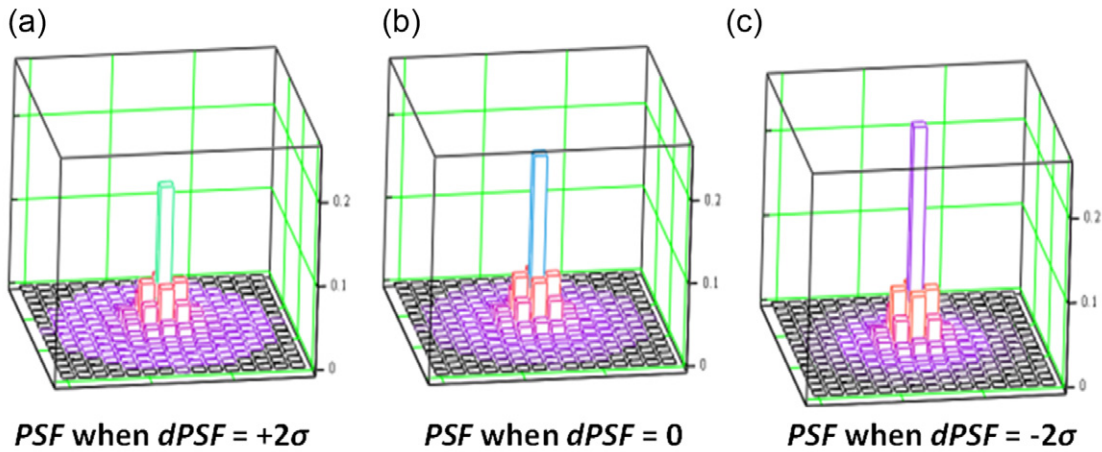


Figure 14. Resulting values for  $PSF$  when (a)  $dPSF$  is  $+2\sigma$ , (b)  $dPSF$  is 0 and (c)  $dPSF$  is  $-2\sigma$ .

$\epsilon_{tool} + d\epsilon_{tool} \leq 1.0$  for each Monte Carlo trial. The distribution for  $d\epsilon_{chip}$  is wider than for  $d\epsilon_{tool}$  since chip emissivity can be influenced by size of source effects, cavities that approximate micro-blackbodies, oxidation, and many other sources of emissivity uncertainty [1].

To simulate error in  $PSF$ ,  $dPSF$  was assigned a normal distribution with a mean of zero and a standard deviation ( $\sigma$ ) of 0.06 per pixel. The 0.06 per pixel standard deviation is a type-B estimation combining the observed variation of the PSF with location and sharpness of focus.

For each Monte Carlo trial, the selected  $dPSF$  is used to modify  $PSF$  by first using equation (17), and then equation (18). Resulting values for  $PSF$  when  $dPSF$  is  $+2\sigma$ , 0 and  $-2\sigma$  are shown in figure 14. When  $dPSF$  is positive, it increases the elements of the PSF matrix in proportion to their distance away from the centre. Equation (18) normalizes  $PSF$  to have a total volume of 1 so that the overall image intensity is not modified by the PSF.

$$PSF_{ij} = PSF_{ij} \cdot (1 + (dPSF \cdot \sqrt{i^2 + j^2})) \quad (17)$$

$$PSF_{ij} = \frac{PSF_{ij}}{\sum_i \sum_j PSF_{ij}} \quad (18)$$

To model relative vibratory motion between the camera and the cutting tool, a  $3 \times 3$  matrix,  $Motion$ , is convolved with the image in the same manner as  $PSF$  in figure 11. For each Monte Carlo trial, values  $dMotion_x$  and  $dMotion_y$  are selected, where each

has a normal distribution and a standard deviation of 0.1 pixel. These are first applied to equation (19) to create a  $3 \times 3$  matrix. Equation (20) is then used to ensure that the average image intensity is not changed.

$$Motion_{ij} = \begin{bmatrix} 0 & \max(0, dMotion_y) & 0 \\ \max(0, dMotion_x) & 1 & \max(0, dMotion_x) \\ 0 & \max(0, dMotion_y) & 0 \end{bmatrix} \quad (19)$$

$$Motion_{ij} = \frac{Motion_{ij}}{\sum_i \sum_j Motion_{ij}} \quad (20)$$

Determination of maximum temperature in an image may be affected by bad pixels in the camera since thermal cameras often have a few bad pixels. To avoid problems associated with bad pixels, the average temperature over a small area of a few pixels in the hottest portion of the image may be used as a definition of the measurand instead of single pixel values. This works well if the size of the hot spot is really a few pixels or larger. However, if the hot spot is small enough, the average of a few pixels may produce a maximum temperature measurement which is ‘biased’ low. The Monte Carlo simulation records maximum temperatures in two ways; the maximum single pixel value and the maximum 3 pixel by 3 pixel average.

**Table 1.** Summary statistics for 1200 trials to characterize the sensitivity of measured maximum temperatures to variations in the error sources (random variables).

Statistic	Error sources							Measured max. true temperature			
	$d\lambda/\mu\text{m}$	$dT_{\text{amb}}/^\circ\text{C}$	$d\varepsilon_{\text{tool}}$	$d\varepsilon_{\text{chip}}$	$dPSF/\text{pixel}^{-1}$	$dMotion_x/\text{pixel}$	$dMotion_y/\text{pixel}$	With PSF correction		No PSF correction	
								1 pixel/ $^\circ\text{C}$	$3 \times 3$ pixel/ $^\circ\text{C}$	1 pixel/ $^\circ\text{C}$	$3 \times 3$ pixel/ $^\circ\text{C}$
Mean	-0.0005	4.24	0.0003	-0.0038	-0.002	0.038	0.042	912.1	873.2	820.7	807.5
Std. error	0.0004	0.16	0.0010	0.0014	0.002	0.002	0.002	0.7	0.5	0.4	0.4
Median	-0.0015	2.52	-0.0001	-0.0025	-0.001	0.000	0.004	911.8	873.1	820.7	807.6
Std. dev. ( $\sigma$ )	0.0148	5.46	0.0341	0.0488	0.061	0.059	0.059	24.7	18.0	14.7	14.2
Sample var.	0.0002	29.79	0.0012	0.0024	0.004	0.003	0.003	608.1	322.8	215.0	200.8
Kurtosis	-1.2260	19.47	-0.1726	0.0096	-0.029	2.749	1.658	0.0	0.1	0.0	0.0
Skewness	0.0580	3.77	0.0642	-0.0040	-0.008	1.757	1.492	0.2	0.1	0.1	0.1
Minimum	-0.0250	0.04	0.01041	-0.1730	-0.209	0.000	0.000	847.0	816.1	772.9	762.2
Maximum	0.0250	52.50	0.1058	0.1420	0.182	0.338	0.318	1009.1	939.7	872.6	858.0

**Table 2.** Linear regression produces coefficients which will ultimately be used in uncertainty analysis.

Fit coefficients			With PSF correction				No PSF correction			
Associated error source	Coefficient name	Units	1 pixel		$3 \times 3$ pixel		1 pixel		$3 \times 3$ pixel	
			Fit value	Standard error	Fit value	Standard error	Fit value	Standard error	Fit value	Standard error
Intercept	$K_{\text{int}}$	$^\circ\text{C}$	917.9	0.15	874.9	0.09	821.4	0.06	808.5	0.05
$d\lambda$	$K_\lambda$	$^\circ\text{C}\mu\text{m}^{-1}$	-161	6.43	-141	3.89	-127	2.45	-124	2.03
$dT_{\text{amb}}$	$K_{\text{amb}}$	$^\circ\text{C}^\circ\text{C}^{-1}$	-0.004 <sup>a</sup>	0.017	0.008 <sup>a</sup>	0.011	0.006 <sup>a</sup>	0.007	0.005 <sup>a</sup>	0.005
$d\varepsilon_{\text{tool}}$	$K_{\varepsilon\text{-tool}}$	$^\circ\text{C}/0.1$	45.3	0.28	42.6	0.17	37.5	0.11	36.2	0.09
$d\varepsilon_{\text{chip}}$	$K_{\varepsilon\text{-chip}}$	$^\circ\text{C}/0.1$	0.8	0.19	0.4	0.12	3.8	0.07	4.9	0.06
$dPSF$	$K_{\text{psf}}$	$^\circ\text{C pixel}$	-271	1.56	-166	0.95	-113	0.59	-107	0.49
$dMotion_x$	$K_{\text{motion-x}}$	$^\circ\text{C}/\text{pixel}$	-178	1.62	-55.3	0.98	-21.1	0.62	-28.4	0.51
$dMotion_y$	$K_{\text{motion-y}}$	$^\circ\text{C}/\text{pixel}$	5.8	1.61	-2.3	0.98	-4.2	0.61	-3.5	0.51
Goodness of fit	$r^2$	none	0.982		0.988		0.993		0.995	

<sup>a</sup> Fit value for  $K_{\text{amb}}$  is not statistically significant due to standard error larger than the fit value, and a  $P$ -value of 0.8

1200 trials of the Monte Carlo simulation were performed. Summary statistics are shown in table 1. The left-hand side of the table quantifies the statistics of the actual samples for each of the random variables. Whether a variable had one-sided variation or symmetric deviations about the mean is most clearly evident from the maximum and minimum values recorded in the last two rows. The right-hand side of the table lists the results for the statistics of the measurand. Results are also included for measured maxima when no PSF correction (deconvolution) is used in the calculation of the true temperature field. The single pixel maximum with PSF correction is of primary interest. However, the maximum 3 pixel by 3 pixel average and the maximum true temperature without PSF correction are also recorded. It can be noted from the mean values that the 1 pixel measured maximum true temperature with or without PSF correction is lower than the maximum true temperature of  $973^\circ\text{C}$  in figure 7(b). In other cases, it may be higher if the estimated emissivity is too low or the estimated PSF is too wide ( $dPSF > 0$ ).

A least-squares linear regression was performed to determine the coefficients of the linear approximation in

equation (21):

$$\begin{aligned} \text{Measured Maximum} = & K_{\text{int}} + K_\lambda d\lambda + K_{\text{amb}} dT_{\text{amb}} \\ & + K_{\varepsilon,\text{tool}} d\varepsilon_{\text{tool}} + K_{\varepsilon,\text{chip}} d\varepsilon_{\text{chip}} + K_{\text{psf}} dPSF \\ & + K_{\text{motion},x} dMotion_x + K_{\text{motion},y} dMotion_y. \end{aligned} \quad (21)$$

In the above equation,  $K_{\text{int}}$  represents the nominal value of measured maximum temperature if there were no variation in the error sources listed in table 1. Shown in table 2, the linear regression gave goodness of fit values,  $r^2$ , ranging between 0.982 and 0.995, indicating good fits. Except for  $K_{\text{int}}$ , the coefficients may be thought of as sensitivities, indicating how much the measured maximum temperature changes for an error in an assumed value. For example,  $K_{\varepsilon,\text{tool}}$  has a value of  $45.3^\circ\text{C}/0.1$  for the 1 pixel maximum which includes PSF correction. Thus, if tool emissivity is incorrect by 0.05, one would expect an error of about  $22.7^\circ\text{C}$  in the measured maximum value.

Note that  $dT_{\text{amb}}$ ,  $dMotion_x$  and  $dMotion_y$  have statistically significant non-zero mean values and/or skewness in table 1. Consider  $dMotion_x$  for example. There is no such thing as 'negative blur', so the mean value for  $dMotion_x$  is non-zero. Also, the measured maximum temperature would

**Table 3.** Standard deviations and sensitivity coefficients of the different sources of uncertainty in maximum tool temperature.

Uncertainty source	With PSF correction						No PSF correction			
			1 pixel		3 × 3 pixel		1 pixel		3 × 3 pixel	
	Standard uncertainty		Sensitivity		Sensitivity		Sensitivity		Sensitivity	
Name	Value	Units	Value	Units	Value	Units	Value	Units	Value	Units
$u(\lambda)$	0.0148	μm	-161	°C μm <sup>-1</sup>	-141	°C μm <sup>-1</sup>	-127	°C μm <sup>-1</sup>	-124	°C μm <sup>-1</sup>
$u(T_{amb})$	5.46	°C	0.004 <sup>a</sup>	°C/°C	0.008 <sup>a</sup>	°C/°C	0.006 <sup>a</sup>	°C/°C	0.005 <sup>a</sup>	°C/°C
$u(\epsilon_{tool})$	0.341	0.1	45.3	°C/0.1	42.6	°C/0.1	37.5	°C/0.1	36.2	°C/0.1
$u(\epsilon_{chip})$	0.488	0.1	0.8	°C/0.1	0.4	°C/0.1	3.8	°C/0.1	4.9	°C/0.1
$U(PSF)$	0.061	pixel <sup>-1</sup>	-271	°C pixel	-166	°C pixel	-113	°C pixel	-107	°C pixel
$u(Motion_x)$	0.059	pixel	-178	°C/pixel	-55.3	°C/pixel	-21.1	°C/pixel	-28.4	°C/pixel
$u(Motion_y)$	0.059	pixel	5.8	°C/pixel	-2.3	°C/pixel	-4.2	°C/pixel	-3.5	°C/pixel

<sup>a</sup> Fit value for  $k_{amb}$  is not statistically significant due to standard error larger than the fit value, and a  $P$ -value of 0.8.

never be increased due to motion blur. Thus, any motion blur will generally result in a lowered measured maximum temperature. This results in the mean of the measured maximum temperatures in table 1 being several degrees lower than the corresponding  $K_{int}$  in table 2.

Note that  $K_{int}$  is several degrees higher than the corresponding mean of the measured maximum temperatures in table 1.  $K_{int}$  equals the mean of the measured maxima only when all the error source distributions ( $d\lambda$ ,  $dT_{amb}$ , etc) are symmetric about zero. As previously mentioned,  $dT_{amb}$ ,  $dMotion_x$  and  $dMotion_y$  were chosen such that their probability distributions had non-zero means and skewness.

Sensitivities associated with  $d\epsilon_{chip}$ ,  $dPSF$ ,  $dMotion_x$  and  $dMotion_y$  ( $K_{\epsilon,chip}$ ,  $K_{psf}$ ,  $K_{motion,x}$  and  $K_{motion,y}$ ) address how one pixel in the sensor array is affected by neighbouring pixel values. It is tempting to assume that sensitivities associated with  $d\lambda$ ,  $dT_{amb}$  and  $d\epsilon_{tool}$  ( $K_{\lambda}$ ,  $K_{amb}$  and  $K_{\epsilon,tool}$ ) are inherently single sensor by nature, and should agree exactly with the single sensor values found analytically in section 3. However, this is not guaranteed to be strictly true in all situations. Section 3 showed that these sensitivities ( $K_{\lambda}$ ,  $K_{amb}$  and  $K_{\epsilon,tool}$ ) are non-linear functions of temperature. Now consider the case where there is a range of different temperatures within a given scenel. The intensities associated with those temperatures are effectively averaged together and interpreted as the apparent temperature for that scenel. However, due to temperature dependence, each intensity within the scenel has a different associated value for sensitivity. Since the reported temperature for a scenel is the result of an average of the intensities, the overall sensitivity for the scenel is a weighted average of the sensitivities, where the weights are determined by the intensities. Fortunately, if emissivity is constant within the scenel, the scenel value for both intensity and sensitivity is dominated by the same brightest (hottest) temperature since it has the most weight. Thus, the sensitivity for the scenel will tend to be ‘close’ to the analytically derived value.

Using the results of Monte Carlo simulation statistics shown in tables 1 and 2, standard uncertainties and their associated sensitivities are summarized in table 3. The standard deviations ( $\sigma$ ) of the uncertainty sources shown in table 1 are used as the estimates of the standard uncertainties ( $u(x_i)$ ) of those variables. The fit coefficients ( $K_i$ ) in

**Table 4.** Typical uncorrected difference between measured and actual maximum temperature.

Difference/°C	With PSF correction		No PSF correction	
	1 pixel	3 × 3 pixel	1 pixel	3 × 3 pixel
Compared to high-resolution image	-55	-98	-152	-165
Compared to camera resolution image	-8	-51	-105	-118

table 2 are listed as estimates for sensitivity of measured maximum temperature to the standard uncertainty. Note that the associated standard error from the linear fit is large compared with  $K_{amb}$ . However, it was clear from the values that  $K_{amb}$  and resulting  $u(T_{amb})$  are very small.

The difference values shown in table 4 compare the actual single pixel maximum for both the high-resolution image and the camera resolution image to the intercept ( $K_{int}$ ) values in table 2. The difference value for the single pixel maximum with PSF correction is -55 °C. This indicates that, considering the high-resolution image as a representative ‘true’ image, the measured maximum temperature will likely be 55 °C lower than the actual maximum. As discussed in section 4, this difference is large because the width of the hot spot is significantly smaller than a scenel in the camera image, causing a sub-pixel size of source error. When very high temperature gradients are present, the measured maximum temperature can be brought closer to the actual value only by increasing the optical magnification. The next row in table 4 compares the measured maxima to the single pixel maximum in the camera resolution image. This indicates the bias if there were no sub-pixel size of source error. In this case, the difference value for the single pixel maximum with PSF correction is -8 °C. This is primarily caused by the error due to  $dMotion_x$  (motion blur) not corrected for in processing the thermal images, which always lowers the maximum temperature measured. If one has an accurate value for motion blur, one may correct for it using the same procedure as the PSF correction. An estimate of motion blur may be gained by using an accelerometer, displacement gauge, or high-speed visible light camera. Another important conclusion from table 4 is that correcting for the blurring due to the PSF is

**Table 5.** Sensitivity coefficients and standard uncertainty components from the numerical and analytical uncertainty analyses.

	Monte Carlo simulation	Analytical	Units
Calibration, $u_{\text{cal}}$	—	0.67	°C
Sensitivity to wavelength, $k_{\lambda}$	−161	−161	°C $\mu\text{m}^{-1}$
Uncertainty component, $u_{\lambda}$	2.4	2.4	°C
Sensitivity to ambient reflected temperature, $K_{\text{amb}}$	−0.004	−0.0003	°C/°C
Uncertainty component, $u_{\text{amb}}$	−0.02	0.0016	°C
Sensitivity to tool emissivity, $K_{\varepsilon,\text{tool}}$	45.3	45.7	°C/0.1
Uncertainty component, $u_{\varepsilon,\text{tool}}$	15.5	15.6	°C
Sensitivity to chip emissivity, $K_{\varepsilon,\text{chip}}$	0.8	—	°C/0.1
Uncertainty component, $u_{\varepsilon,\text{chip}}$	0.4	—	°C
Sensitivity to PSF, $K_{\text{psf}}$	−271	—	°C pixel
Uncertainty component, $u_{\text{psf}}$	16.5	—	°C
Sensitivity to X-motion blur, $K_{\text{motion},x}$	−178	—	°C/pixel
Uncertainty component, $u_{\text{motion},x}$	10.5	—	°C
Sensitivity to Y-motion blur, $K_{\text{motion},y}$	5.8	—	°C/pixel
Uncertainty component, $u_{\text{motion},y}$	0.3	—	°C
Combined standard uncertainty for single-pixel maximum $T_{\text{true}} = 912.15$ °C:			
No correlation: $u_c = 25.1$ °C			
Full correlation: $u_{c,\rho=1} = 46.3$ °C			

essential to obtain an accurate measurement of the maximum temperature.

## 6. Combined uncertainty

The standard uncertainty of each input variable and the magnitude of its sensitivity coefficient shown in table 3 are multiplied together to obtain the standard uncertainty in temperature due to that variable,  $u_i = |K_i| \cdot u(x_i)$ , and these are listed in table 5. For instance, the standard uncertainty in wavelength  $u(\lambda_0) = 0.015 \mu\text{m}$  is multiplied with its sensitivity coefficient  $|K_i| = 161 \text{ °C } \mu\text{m}^{-1}$  to obtain  $u_i = 2.39 \text{ °C}$ . Note from figure 13 that  $u(\lambda_0)$  and  $u(T_{\text{amb}})$  are not assumed normal distributions, but the standard deviation of the samples is used to define their respective standard uncertainty. Calibration coefficients and uncertainty components from the analytical approach are calculated from the functions that generated figure 2 through figure 4.

Given these inputs, table 5 gives the standard uncertainty components used to calculate the combined standard uncertainty for the example measurement given in section 5. It can be seen that uncertainties due to PSF, tool emissivity and motion in the X direction are the three largest standard uncertainty components. Since the numerical and analytical approach produced components of standard uncertainty that are in good agreement as shown in table 5 for variables where both are available, values from the Monte Carlo simulation are used to form the combined uncertainty.

In the introduction, equation (1) presented the combined uncertainty calculation in the absence of correlated variables. In reality, some of the input variables are correlated to some degree. Determining this correlation will require replacing the linear model in equation (21) with a non-linear model and a much larger number of simulations. Rather than measuring or assuming correlations, Minkina and Dudzik calculated combined uncertainty for a variety of estimated correlations between all their model input variables [15]. They found that of all the tested correlations, the combined standard

uncertainty is affected most by the correlation between emissivity and reflected radiance from ambient sources. Neglecting this correlation may over- or underestimate the combined uncertainty by up to 1%. The worst-case scenario yielding the largest calculated combined uncertainty occurs if all correlation terms are positive. For the case of perfect correlation of all variables in a manner yielding the highest  $u_c$ , the combined standard uncertainty is the square of the sum of each of the individual standard uncertainties:

$$u_c(T)^2 = u_{\text{cal}}^2(T) + \sum_{i=1}^N u_i^2 + 2 \sum_{i=1}^{N-1} \sum_{j=i+1}^N u_j u_i \rho(x_i, x_j)$$

$$u_{c,\rho=1}(T)^2 = \left( u_{\text{cal}}(T) + \sum_{i=1}^N u_i \right)^2 \quad \text{for } \rho(x_i, x_j) = 1. \quad (22)$$

Table 5 lists the combined uncertainty for no correlations (best-case scenario, equation (1)), as well as the combined uncertainty for positive correlations affecting every variable pair (worst-case scenario, equation (22)).

For a coverage factor of  $k = 2$ , the expanded uncertainty for the non-correlated case is  $U(T_{\text{true}}) = 50.1 \text{ °C}$ , and for the worst-case scenario involving perfect correlation  $U(T_{\text{true}}) = 92.5 \text{ °C}$ . Minkina and Dudzik also concluded that correlation between emissivity and ambient temperature had the highest effect on uncertainty compared with other correlations [15]. Given the very low standard uncertainty of ambient temperature  $u(T_{\text{amb}})$  in table 3, correlations with  $T_{\text{amb}}$  would contribute little to the combined uncertainty in equation (22). Therefore, the true expanded uncertainty is likely closer to that assuming no correlations.

## 7. Discussion

For microscopic thermography of targets with relatively large temperature gradients around small areas of interest, PSF measurement and deconvolution is recommended. Without it, the peak temperature can be biased significantly lower

by as much as 150 °C for the measurement conditions used here. When performing thermographic imaging of ‘hot spots’ smaller than the scene size, the measured temperature is biased lower than the true peak temperature of the object. Under the measurement conditions used here, blurring by the PSF is the biggest contributor to error causing the measured maximum temperature to be lower than the actual maximum temperature by about 50 °C. For this reason, it is compensated by incorporating PSF deconvolution. Size of source effects stemming from sub-scene hot spots cannot be corrected through deconvolution.

According to the GUM, measurement bias should be corrected for if known and the uncertainty of that correction factor added to the uncertainty budget. In the example measurement of section 5, PSF deconvolution is the only ‘known’ corrective factor, and is accounted for in the budget in table 5. However, the uncertainty in PSF correction becomes the biggest source of uncertainty, higher than even the uncertainty due to emissivity, which is usually considered to be the source of the largest uncertainty. If the PSF is characterized well, and some method of achieving repeatable focus is adopted, this component of uncertainty can be decreased. Motion blur may also be corrected using deconvolution similar to PSF, if the motion is known with very low uncertainty.

The best way to reduce the bias due to size of source effects is to decrease the scene size to approach the scale of the ‘hot spot’, or simply put, increase the magnification of the system. The magnification is limited, however, by the wavelength of the IR radiation measured, which sets the diffractive limit or minimum possible resolution of the optics system. Higher magnification also increases the motion blur (assuming the same motion exists) with respect to the scene size, narrows the depth of field thus increasing the risk of unfocused blur, and reduces the incident radiant flux on each pixel. Due to the lower flux, longer integration times are necessary, which further increase any motion blur. In short, higher magnification will decrease the inherent bias, though camera sensitivity also needs to be increased as well to reduce the necessary integration time.

Uncertainty components depend heavily on the attributes of the camera, the measured thermal scene and definition of the measurand. The combined uncertainty statement given is strictly applicable only to the particular attributes considered here. However, the procedure(s) outlined here to determine the measurement uncertainty are applicable to other similar IR thermographic measurements.

## 8. Conclusions

Analytical and numerical approaches were used to characterize the uncertainty of IR thermographic measurement of the maximum temperature of metal cutting tools. Some salient features are as follows:

- (1) A simple procedure is given for estimating uncertainty stemming from thermal camera calibration. This is based on the standard error of estimate of a least-squares fit of the Sakuma–Hattori equation to calibration data. The Sakuma–Hattori fit allows for uncertainty analysis through analytical means.
- (2) Both analytical and numerical methods are used to determine the standard uncertainties arising from three input variables, namely the central wavelength of the camera spectral responsivity, tool emissivity and ambient reflected temperature. Both methods gave results in close agreement for these uncertainty components.
- (3) The numerical method makes it easy to calculate standard uncertainties due to variation of emissivity over the scene, PSF and motion blur, which otherwise are not easy to calculate, and have not been discussed in the metal cutting literature. In addition, the Monte Carlo method is more flexible in that it can use different probability distributions for the measurement variables such as log-normal or uniform distributions.
- (4) The analytical method can easily show how components of uncertainty vary with measured temperature and process variables by providing algebraic solutions that detail the non-linear interactions among the variables, over a wide range of these variables. These complex relationships can be communicated through plots similar to figure 4 through figure 6.
- (5) The two highest sources of uncertainty are from the tool emissivity and point spread function. Emissivity is regarded as the source of highest thermographic measurement uncertainty in most of the literature [4], but it is shown here that PSF can contribute to uncertainty on the same order of magnitude as emissivity. It is believed that this is the first study discussing measurement uncertainty of peak tool temperatures due to PSF. For microscopic thermography of targets with relatively large temperature gradients around small areas of interest, PSF measurement and deconvolution are recommended to compensate for the bias induced by the PSF. Additionally, increasing the spatial resolution, by increasing the magnification and/or the sharpness of the PSF, will help reduce the measurement uncertainty.
- (6) For the example thermographic scene given in figure 7, the expanded measurement uncertainty for the PSF-corrected, single pixel maximum temperature is  $U = 50.1\text{ °C}$  ( $k = 2$ ), neglecting correlations among the variables. This corresponds to a relative expanded uncertainty of about 4% (for the example scene in kelvin).

## Acknowledgments

The authors gratefully acknowledge Steve Mates of the Material Science and Engineering Division at NIST for loaning the COTS infrared camera used in this work. Special gratitude is given to Shawn Moylan, Kevin Jurens and Howard Yoon at NIST for their review and feedback. Much gratitude is also given to the article referees selected by the journal who provided especially detailed, insightful and helpful feedback.

## References

- [1] Whitenton E P 2010 High-speed dual-spectrum imaging for the measurement of metal cutting temperatures *NIST Interagency/Internal Report (NISTIR) 7650*

- [2] Whitenton E P 2012 An introduction for machining researchers to measurement uncertainty sources in thermal images of metal cutting *Int. J. Mach. Mach. Mater.* **12** 195–214
- [3] Abukhshim N A, Mativenga P T and Sheikh M A 2006 Heat generation and temperature prediction in metal cutting: a review and implications for high speed machining *Int. J. Mach. Tools Manuf.* **46** 782–800
- [4] Davies M, Ueda T, M'saoubi R, Mullany B and Cooke A 2007 On the measurement of temperature in material removal processes *CIRP Ann. Manuf. Technol.* **56** 581–604
- [5] Komanduri R and Hou Z B 2001 A review of the experimental techniques for the measurement of heat and temperatures generated in some manufacturing processes and tribology *Tribol. Int.* **34** 653–82
- [6] BIPM, IEC, IFCC, ISO, IUPAC, IUPAP and OIML 1995 *Guide to the Expression of Uncertainty in Measurement (GUM)* (Geneva: International Organization for Standardization)
- [7] Miller M R, Mulholland G and Anderson C 2003 Experimental cutting tool temperature distributions *J. Manuf. Sci. Eng.* **125** 667–73
- [8] Madding R P 1999 Emissivity measurement and temperature correction accuracy considerations *Proc. SPIE* **3700** 393–401
- [9] Outeiro J C, Dias A M and Lebrun J L 2004 Experimental assessment of temperature distribution in three-dimensional cutting process *Mach. Sci. Technol.* **8** 357–76
- [10] Davies M, Yoon H, Schmitz T, Burns T and Kennedy M 2003 Calibrated thermal microscopy of the tool–chip interface in machining *Mach. Sci. Technol.* **7** 167–90
- [11] Taylor B N and Kuyatt C E 1994 Guidelines for evaluating and expressing the uncertainty of NIST measurement results *NIST Technical Note* 1297
- [12] Ivester R W 2011 Tool temperatures in orthogonal cutting of alloyed titanium *Trans. NAMRI-SME (Corvallis, OR, 14–17 June 2011)* pp 253–9
- [13] Arriola I, Whitenton E, Heigel J and Arrazola P 2011 Relationship between machinability index and in-process parameters during orthogonal cutting of steels *CIRP Ann. Manuf. Technol.* **60** 93–6
- [14] Minkina W and Dudzik S 2006 Simulation analysis of uncertainty of infrared camera measurement and processing path *Measurement* **39** 758–63
- [15] Minkina W and Dudzik S 2009 *Infrared Thermography: Errors and Uncertainties* Wiley Online Library
- [16] Saunders P *et al* 2008 Uncertainty budgets for calibration of radiation thermometers below the silver point *Int. J. Thermophys.* **29** 1066–83
- [17] Heigel J C and Whitenton E P 2010 The effects of emissivity and camera point spread function on the temperature measurement of segmented chip formation using infrared thermography *Proc. ASME-MSEC (Erie, PA, 12–15 October 2010)*.
- [18] DeWitt D P and Nutter G D 1988 *Theory and Practice of Radiation Thermometry* Wiley Online Library
- [19] McCluney W R 1994 *Introduction to Radiometry and Photometry* vol 1 (Boston, MA: Artech House)
- [20] Walach T 2008 Uncertainty in temperature infrared measurements of electronic microcircuits *15th Int. Conf. on Mixed Design of Integrated Circuits and Systems (Poznan, Poland, 19–21 June 2008)* pp 359–63
- [21] Sakuma F and Hattori S 1982 Establishing a practical temperature standard by using a narrow-band radiation thermometer with a silicon detector *Temperature: its Measurement and Control in Science and Industry* vol 5 ed J F Schooley (New York: AIP) pp 421–7
- [22] ASTM Standard E2847-11 2011 *Standard Practice for Calibration and Accuracy Verification of Wideband Infrared Thermometers* (West Conshohocken, PA: ASTM International)
- [23] Saunders P 2009 Calibration of low-temperature infrared thermometers *MSL Technical Guide* 22, Measurement Standards Laboratory of New Zealand Contract No 22
- [24] 2008 *Altair Reference Guide DL002U-D Cedip Infrared Systems*, FLIR Systems Inc.
- [25] 2013 *The Ultimate Infrared Handbook for R&D Professionals* FLIR Systems Inc.
- [26] Saunders P 2003 Propagation of uncertainty for non-linear calibration equations with an application in radiation thermometry *Metrologia* **40** 93
- [27] Saunders P and White D R 2003 Physical basis of interpolation equations for radiation thermometry *Metrologia* **40** 195
- [28] Saunders P and White D R 2003 Interpolation errors for radiation thermometry *Metrologia* **41** 41
- [29] Saunders P 1997 General interpolation equations for the calibration of radiation thermometers *Metrologia* **34** 201
- [30] Baer R L 2004 Circular-edge spatial frequency response test *Proc. SPIE* **5294** 71–81
- [31] Boreman G D and Yang S 1995 Modulation transfer function measurement using three- and four-bar targets *Appl. Opt.* **34** 8050–2
- [32] Nill N B 2001 Conversion between sine wave and square wave spatial frequency response of an imaging system *MITRE Corp Technical Report*
- [33] Heigel J C and Whitenton E P 2009 The effects of integration time and size-of-source on the temperature measurement of segmented chip formation using infrared thermography *Proc. ASME-MSEC (West Lafayette, IN, 4–7 October 2009)*